Structural Engineering and Mechanics, *Vol. 66, No. 6 (2018) 713-727*
DOI: https://doi.org/10.12989/sem.2018.66.6.713

Energy absorption of the ring stiffened tubes and the application in blast wall design

JinJing Liao[*1,3] and Guowei Ma[2,3a]

[1]*Atkins Australasia Pty Ltd., Level 8, 50 St Geroges Terrace, Perth WA 6000, Australia*
[2]*School of Civil and Transportation Engineering, Hebei University of Technology, Tianjin 300401, China*
[3]*School of Civil, Environmental and Mining Engineering, The University of Western Australia, 35 Stirling Hwy, Crawley WA 6009, Australia*

(Received February 5, 2018, Revised March 20, 2018, Accepted March 21, 2018)

Abstract. Thin-walled mental tubes under lateral crushing are desirable and reliable energy absorbers against impact or blast loads. However, the early formations of plastic hinges in the thin cylindrical wall limit the energy absorption performance. This study investigates the energy absorption performance of a simple, light and efficient energy absorber called the ring stiffened tube. Due to the increase of section modulus of tube wall and the restraining effect of the T-stiffener flange, key energy absorption parameters (peak crushing force, energy absorption and specific energy absorption) have been significantly improved against the empty tube. Its potential application in the offshore blast wall design has also been investigated. It is proposed to replace the blast wall endplates at the supports with the energy absorption devices that are made up of the ring stiffened tubes and springs. An analytical model based on beam vibration theory and virtual work theory, in which the boundary conditions at each support are simplified as a translational spring and a rotational spring, has been developed to evaluate the blast mitigation effect of the proposed design scheme. Finite element method has been applied to validate the analytical model. Comparisons of key design criterions such as panel deflection and energy absorption against the traditional design demonstrate the effectiveness of the proposed design in blast alleviation.

Keywords: ring stiffened tube; blast wall; flexible support; energy absorption; analytical model; finite element analysis

1. Introduction

Blast walls have been widely used in civil and military sectors to mitigate explosion effects (Al-Rifaie and Sumelka 2017). Based on structural global behaviours and design philosophy, blast walls can be generally categorised into two groups: strong and soft structural forms. Strong forms rely on high strength and stiffness to resist imposed loads, such as concrete structures. Soft structures adopt an opposite approach known as energy absorption, in which most of the blast energy is dissipated in form of plastic deformation, material strain hardening effects, strain-rate effects (Lu and Yu 2003).

Among all energy absorbers, thin-walled mental tubes have attracted numerous research attentions due to their low cost, easy fabrication and excellent energy absorption capability (Eyvazian *et al*. 2014). Typically, thin-walled mental tubes are usually crushed axially and laterally for energy dissipation, which results in two types of force-deflection responses known as “steeply falling” for axial crushing and “flat-topped” for lateral crushing as shown in Fig. 1 (Lu and Yu 2003). For axial crushing, because of the sudden drop after the initial peak in the curve, its crushing force efficiency (the ratio of mean over peak crushing force) is relatively low. Moreover, it is also very sensitive to the impact velocity. Therefore, by comparison, tubes under lateral crushing are more desirable and reliable energy adaption devices due to the higher crushing force efficiency and the constant plateau crushing force over a long stroke (Fan *et al*. 2013). However, there is a major drawback of tube lateral crushing that plastic hinges can form easily in the thin cylindrical wall, which limits its energy absorption performance. Several studies have been carried out to improve its performance. Wang *et al*. (2015) studied an internally nested circular tube system with two tubes of smaller diameters stacked inside a bigger tube. Fan *et al*. (2013) designed sandwich tubes filled with aluminium foam. Both studies have successfully enhanced the energy absorption. However, their designs may not be weight-wise due to the introduction of large amount of additional materials. Nouri *et al*. (2015) examined the impact resistances of tubes made from expanded mental sheets which have very light weight but effective collapse mechanism, however, this collapse mechanism is anisotropic when subjected to lateral crushing.

This study proposes a simpler, lighter but more efficient energy absorption device called the ring stiffened tube, which is shown in Fig. 2(b). The cylindrical tube wall is stiffened by T-stiffener all along its perimeter, which can substantially increase the bending capacity of the tube wall and thus delay the formation of plastic hinges during lateral crushing. In addition, the flange of the T-stiffener can

∗Corresponding author, Structural Engineer and MPhil Student
E-mail: LiaoJin507@gmail.com
[a]Professor
E-mail: Guowei.Ma@uwa.edu.au

http://www.techno-press.com/journals/sem&subpage=7
ISSN: 1225-4568 (Print), 1598-6217 (Online)

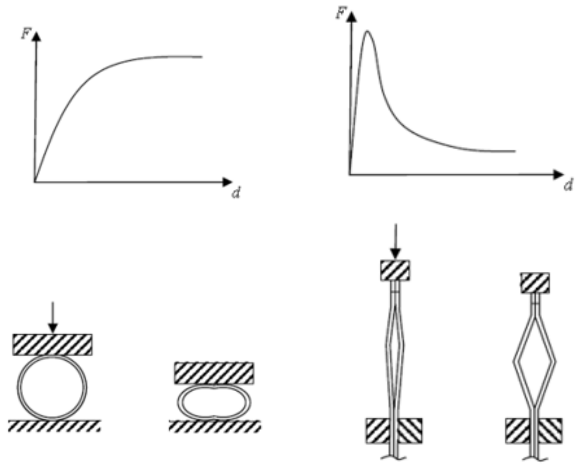

(a) "Flat-topped" (b) "Steeply failing"

Fig. 1 Force-deflection responses for two kinds of energy absorption devices (Lu and Yu 2003)

prevent the stiffener web from lateral or local buckling so that the stiffener itself become very rigid and thus can provide consistent bending enhancement during the crushing without compromise. As less materials are introduced, the weight-efficiency of this new device is high. Similar designs have been widely used in joints of offshore jacket-type platforms to resist punching shear. However, its energy absorption capability under impact or blast has yet to be investigated.

The application of thin-walled mental tubes in protective structures has also been studied extensively, however, the majority of the investigations focus on using tubes as cores of sandwich panels (Xia *et al*. 2016) or sandwich beams (Xiang *et al*. 2016). There is very few study investigating the blast alleviation effects by placing thin-walled tubes at the supports of protective structures. To this end, the other purpose of this study is to fill this research gap by performing a feasibility study of using the stiffened thin-walled tubes as flexible supports for the blast wall design. Besides, a third energy absorber (i.e., spring, additional to the panel and the tube) is introduced to the system to provide additional energy absorption capability. Inspired by this triple energy absorbers concept, a hybrid blast barrier system has taken shape by introducing energy absorption devices at the supports.

Current interests on anti-blast research focus on the blast alleviation effects of utilizing new materials with light weigh but high strength, such as ultra-high molecular weight polyethylene fiber (Zhang *et al*. 2017). In addition, Meng *et al*. (2016) and Zhang *et al*. (2018) investigated the blast resistance enhancement of a panel under the combined effects of new material (i.e., sheet molding compound material reinforced by carbon fiber reinforced plastic) and new structural configuration (i.e., hierarchical layout of stiffeners). Significant enhancements can be achieved provided that the connections at the panel supports do not compromise, as they become "the short board of the bucket". In traditional design, blast wall is a monolithic structure whose end connections are consist of welded end plates extended from the supporting plate girders. For the proposed design scheme, instead of end plates, energy absorption devices will be installed between the supporting steelwork and the blast wall panel to form a flexible support as shown in Fig. 2(a), which is also a new structural configuration. The devices can be welded to both girders and panels at site. It is comprised of three parts: sliding core, roller core and the outer crust that all are made of steel as in Fig. 2(a). There are voids or gaps between these three components and hence it has certain degree of freedom to slide and rotate at the same time, which is specially designed against mode II (tensile) and mode III (shear) failures (Menkes and Opat 1973) of a monolithic blast wall. Improvements have been made to increase its energy absorption capability by filling the sliding voids with ring stiffened tubes and constraining the roller core with linear springs. Thereby, the sliding core of the support together with the blast wall panel can move back to relieve the blast load. Meanwhile, blast energy can be dissipated through the tube crushing. Another advantage of the application of the tubes is that its "flat-topped" crushing behaviour (i.e., the crushing force plateau over a long stroke) can act as a cushion to prevent or delay sudden and rapid increase of shear reaction forces, which can greatly reduce the likelihood of weld shear failure. The linear springs around roller core provides substantial resistances to prevent large support rotation especially during strong blasts.

In the present study, evaluation of the energy absorption performance of the ring stiffened tube is presented first. With the force-displacement curves of the crushing tubes, an analytical model is developed to investigate the blast alleviation effects of the proposed system in terms of panel deflection and energy absorption. The results are also collaborated with numerical findings in order to validate the analytical model.

2. Energy absorption of the ring stiffened tube

2.1 Specimen description

Finite element (FE) method is applied to evaluate the energy absorption performances of the ring stiffened tubes. A number of tube crushing studies (Fan *et al*. 2013, Wang *et al*. 2015) involved both experimental and numerical methods have verified that FE simulations can yield corroborative results with experiments with less costs. There are four tubes tested, one empty tube and three tubes with ring stiffeners at different spacings, namely, R1, R3, and R5. All tubes are with the same outer diameter (OD) × wall thickness (WT) as 100 mm × 2.5 mm, and a length of 100 mm. Their dimensions and sketches are shown in Fig. 3.

2.2 Finite element model

ABAQUS/Explicit (SIMULIA 2015) is used to perform the crushing simulations. The tubes are modelled by S4R element with five integration points through the thickness. The mesh sizes of the models are kept the same as their wall thickness, a range of 5040 to 8820 total elements are used to model the four tubes. The tubes are rested between

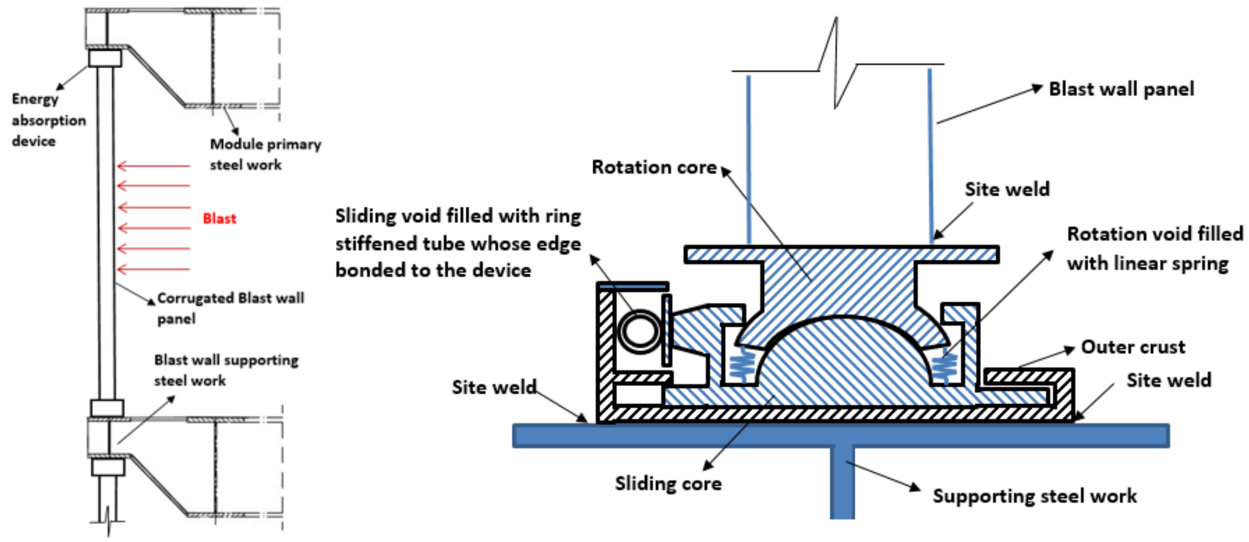

(a) Blast wall side view and energy absorption device at the support

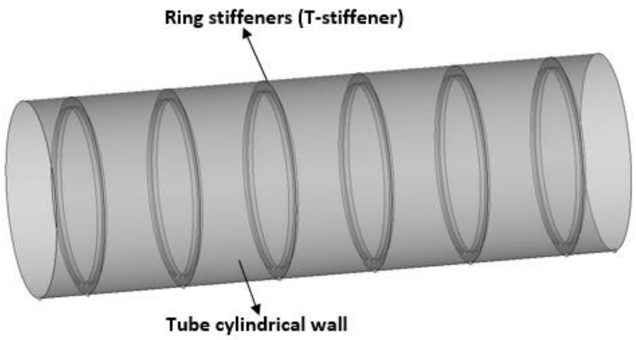

(b) Isometric view of a ring stiffened tube

Fig. 2 The proposed hybrid blast barrier system

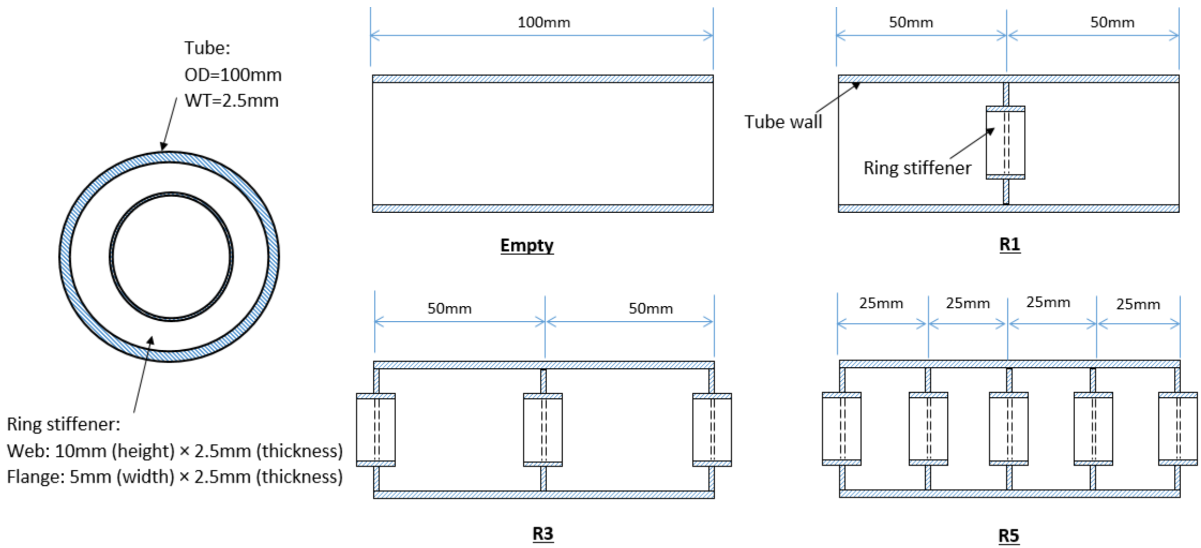

Fig. 3 Cross section geometry of specimens

two rigid body plates, the bottom base is fixed and a total vertical displacement of 100 mm are gradually applied to the top plates to crush the tubes, as illustrated in Fig. 4(a). General contact algorithm is defined to simulate the interaction between tubes and two plates. Nonlinear geometry is turn on to capture the large deformation and second order effects.

2.3 Material model

The material for the tubes is mild steel S235. It has the Young's modulus of 210 GPa, Poisson's ration of 0.3 and

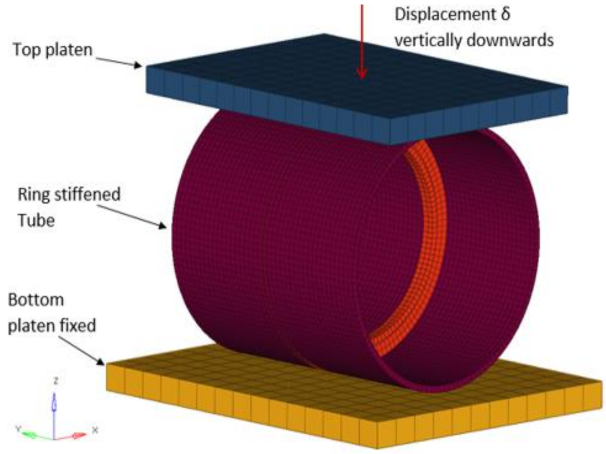

(a) Finite element model of the specimen R1

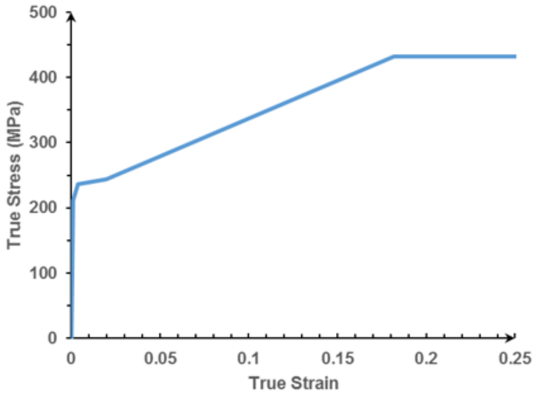

(b) True stress-strain curve of S235 mild steel

Fig. 4 Finite element and material model

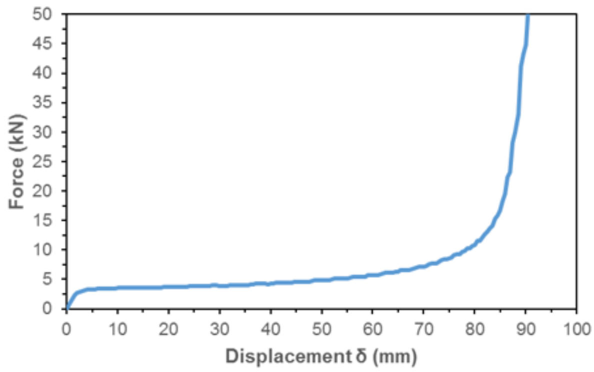

(a) Force-displacement curve

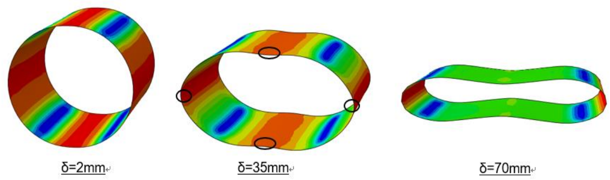

(b) Deformed shapes

Fig. 5 Force-displacement curve and deformed shapes – Empty

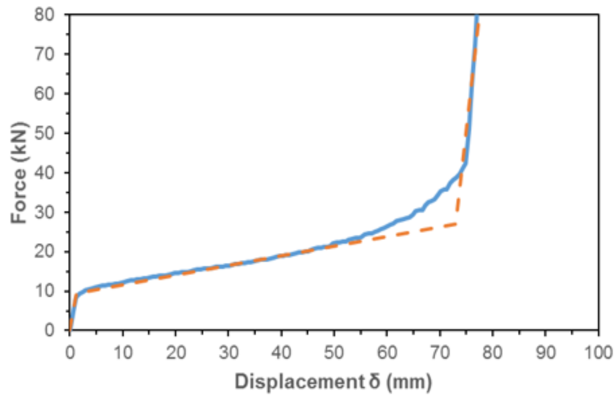

(a) Force-displacement curve

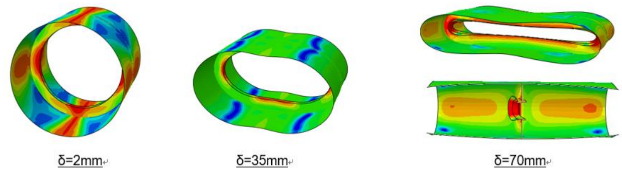

(b) Deformed shapes

Fig. 6 Force-displacement curve and deformed shapes-R1

density of 7850 kg/m^3. The true stress-strain curve (shown in Fig. 4(b)) recommended by DNV-RP-C208 (2013) for S235 is adopted, in which the initial yield stress is 236.2 MPa.

2.4 Results and discussion

2.4.1 Force-displacement curves and deformed shapes

The force-displacement curves and deformed shapes of the four specimens are shown in Fig. 5 to Fig. 8. Tri-linear dash lines in the figures are used to capture their compressive behaviours for the calculations in Section 3 of this paper. Deform shapes at three crushing displacements (δ=2, 35 and 70 mm) are depicted for each tube.

As shown in Fig. 5 for an empty tube, the early plastic hinge formations in the four circled locations combined with the strain localisation effect prevent it from further energy absorption, and hence the force-displacement curve is relatively flat with a small peak crushing force of 3.18 kN at a displacement about 3 mm. Further crushing to δ=70 mm, the deformed shape similar to a "∞" shape resembles closely with the previous experimental findings (Lu and Yu 2003).

For the ring stiffened tubes, the forces-displacement curves and deformed shapes are relatively different because the failure mechanism has changed. Due the increase of the second moment of inertia of the tube wall section with the T-stiffeners, the first peak crushing forces have been significantly increased. It is evident that plastic hinge formations have been delayed or even prevented when comparing the deformed shapes at δ=35 mm between stiffened and empty tubes, in which ring stiffened tubes deform into elliptical shapes. This is because the governing failure mechanism has shifted from plastic hinge formation in the cylindrical wall to the failure of the stiffeners. Furthermore, the flange of the stiffeners can restrain the stiffener web from local or lateral buckling, which makes it very rigid. This can be verified by looking at the tube

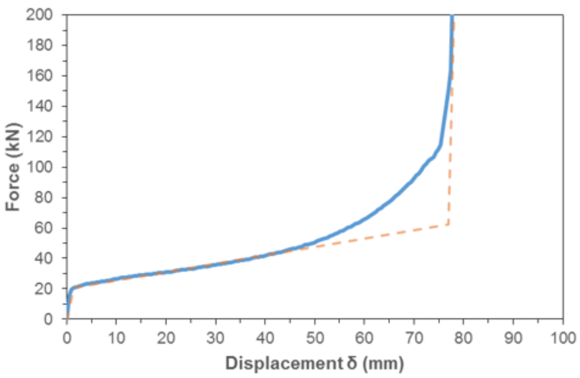

(a) Force-displacement curve

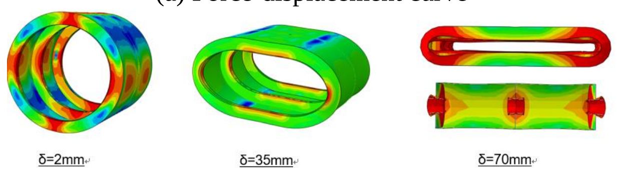

(b) Deformed shapes

Fig. 7 Force-displacement curve and deformed shapes-R3

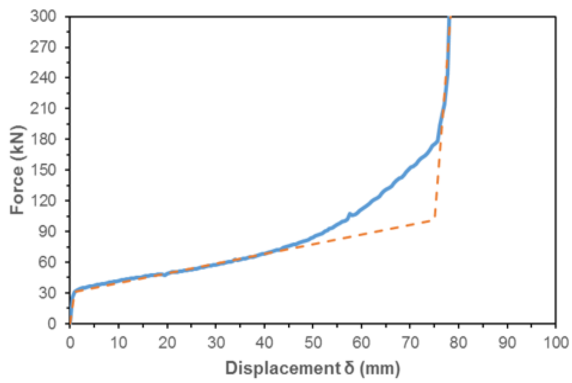

(a) Force-displacement curve

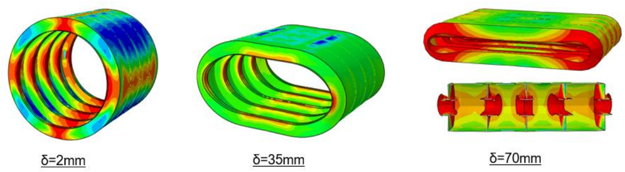

(b) Deformed shapes

Fig. 8 Force-displacement curve and deformed shapes-R5

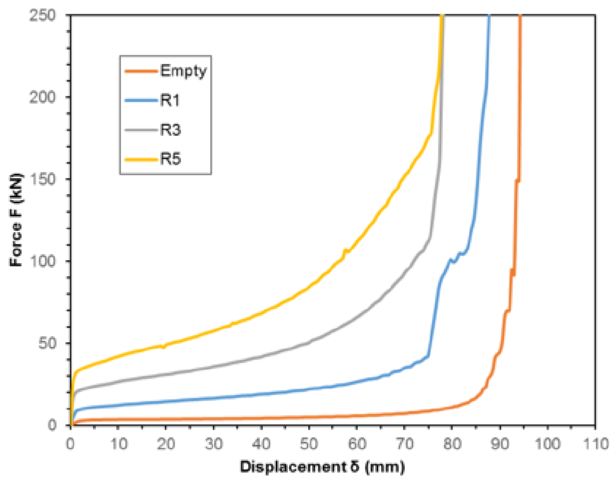

(a) Force-displacement curves

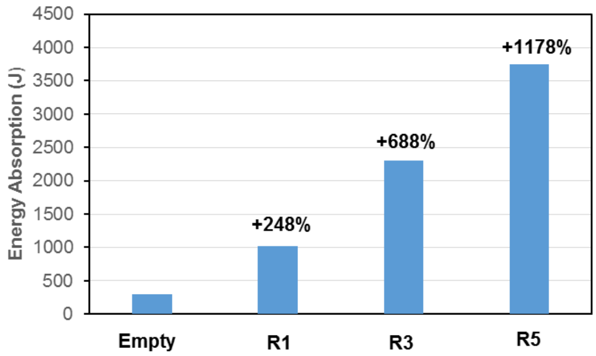

(b) Energy absorption bar charts

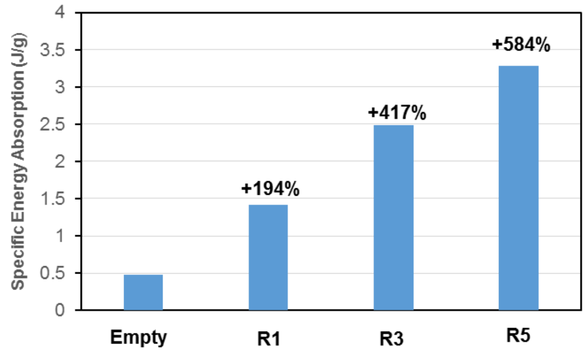

(c) Specific energy absorption bar charts

Fig. 9 Comparison of energy absorption performance

cross-section views at δ=70 mm, in which the stiffeners remain relatively intact. Without compromise, the stiffeners can provide consistent bending capacity to the tubes so that an increasing trend rather than crushing plateau is observed in the crushing zone of the force-displacement curve. The hardening stiffness of the curves are about 1/30 of the initial stiffness based on the dash line approximation. As state before, this implies the crushing force efficiency of the ring stiffened tubes is extremely high and tubes are capable to absorb more energy. However, the stroke of ring stiffened tube becomes shorter at 75 mm, which is the distance between top and bottom stiffeners.

2.4.2 Energy absorption performance

Generally, there are many key parameters to evaluate the energy absorption performance of a device (Lu and Yu 2003), amongst, the peak crushing force, energy absorption and specific energy absorption are very representative and thus adopted in this study.

Peak crushing force (PCF) is defined as the first maximum load in the force-displacement curve. Energy absorption (EA) is the energy dissipated by the device during crushing, which can be determined from the area under the force-displacement curve up to 80% of the stroke i.e., EA= $\int_0^{0.8\delta} F{\cdot}d\delta$. Specific energy absorption (SEA) is the energy absorption divided by the mass of the device i.e., SEA=EA/mass, indicating that the greater the value is, the more weight-efficient the device is.

The force-displacement curves of the four tubes are

Table 1 Energy absorption performances of four tubes

Tube	Mass (g)		PCF (kN)		EA (kJ)		SEA(J/g)	
	value	INC.	value	INC.	value	INC.	value	INC.
Empty	610	\	3.29	\	0.29	\	0.48	\
R1	720	18%	9.40	185%	1.02	248%	1.41	194%
R3	930	52%	19.44	511%	2.31	688%	2.48	417%
R5	1140	87%	31.10	844%	3.74	1178%	3.28	584%

plotted for comparison in Fig. 9. As described above, PCF increases significantly with the increase of ring stiffener number, they are 9.4 kN for R1, 19.44 kN for R5 and 31.1 kN for R5 at displacements approximate 1 mm as summarised in Table 1. Remarkably for R3 and R5 tubes, the PCFs rise up to about 6 and 9 times of the empty tube respectively. In addition, as the number of ring stiffeners increases, it is noticed that the initial stiffness of the curves becomes steeper, which indicates that by adjusting the spacing of the ring stiffeners the energy absorption capability of the tubes can be graded for different blast intensities.

EA and SEA of the four tubes are also summarised in Table 1 and plotted in Fig. 9 for comparison, the percentages of increase (INC.) compared to the empty tube are labelled above the bar charts. Similar to PCF, substantial increases are observed with the increasing number of ring stiffeners. Especially for R3 and R5 cases, by simply adding 3 and 5 strips of ring stiffeners, the energy absorption capacities of the tubes can be enhanced by 7 times (for R3) and 11 times (for R5) compared to the empty tube. From a weight-wise point of view, with just 58% (for R3) and 87% (for R5) increases in mass, the SEA values are 2.48 and 3.48 J/g for R3 and R5 respectively, which have increased by 4 and almost 6 times compared to an empty tube with a SEA value of 0.48.

In summary, due to the increase in bending capacity of the tube wall section and restraining effect of the stiffener flange, plastic hinge formations on tube walls are effective delayed or prevented and thus energy absorption performance is substantially enhanced with less added materials. The potential application of the ring stiffened tubes as energy absorption supports for an offshore blast wall is investigated in the next section.

3. Application in blast wall design

3.1 Analytical modelling

3.1.1 Overview

This section aims to develop an analytical model to study the blast alleviation effects of the proposed system shown in Fig. 2. The structural responses under linear spring supports have been investigated (Chen *et al*. 2011, Song *et al*. 2014). It is found out that peak responses can be delayed but not reduced, as energy is stored rather than absorbed. In addition, in order to delay the peak responses, the stiffness of the linear soft support shall be relatively small, which will result in large support displacements that

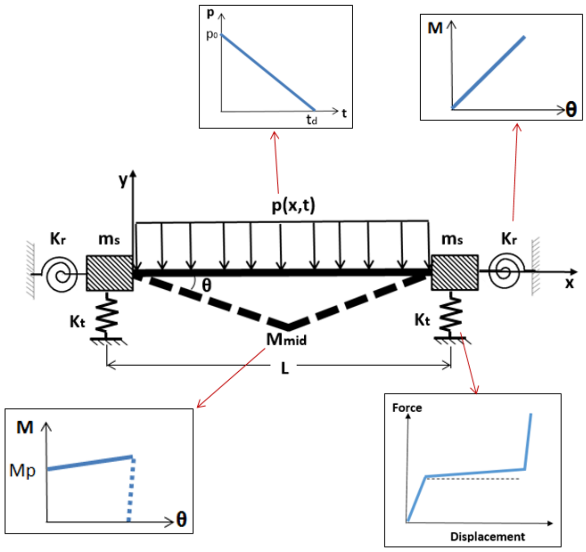

Fig. 10 An overview of the analytical model

hinders its practicality in engineering design.

The present study proposes using the ring stiffened tubes as energy absorbers at supports, therefore the theoretical model of linear spring supports have been further advanced to account for elastic compression, crushing and unloading behaviour of the tube. Efforts are also made to incorporate the material nonlinearity such as strain hardening of steel after plastic hinge formation so that both the maximum and permanent (plastic) deflections can be predicted by this improved model. However, the effect of axial restraint and corresponding geometry nonlinearity are not considered in this model. This is deemed conservative in the preliminary design stage. Friction effect is considered to be minimal and hence neglected in this study. Damping is usually conservatively ignored in blast-resistant design, the reasons are two folds. On the one hand, under blast and high-speed impact load (loadings are usually applied in milliseconds), the structure might not have time to dissipate the shock energy through its dynamic vibrations. On the other hand, although damping comes into effect in the free vibration stage, it is normally not the area of interest because peak responses usually occur in the forced vibration stage.

The corrugated blast wall panel is simplified as a beam that the supports are simplified as two sets of springs (translational and rotational). An overview of the analytical model is shown in Fig. 10. The beam length is denoted as L, unit length mass as m. K_t is the stiffness of the translational spring, K_r is the stiffness of the rotational spring, and m_s is the mass for each support.

3.1.2 Beam elastic stage

In elastic stage, the beam deflection can be derived with the simultaneous beam vibration governing equation and the equation of motion.

The blast loading can be defined as in Eq. (1), where p_0 is the peak blast loading magnitude, $F(t)$ is the blast loading time characteristic function, $f(x)$ is blast loading distribution function. t is time starting from the arrival of the blast load

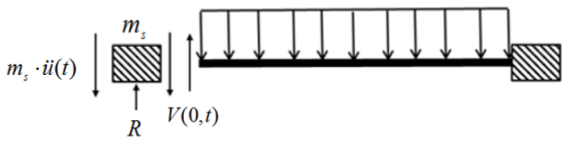

(a) Free body diagram at the left support

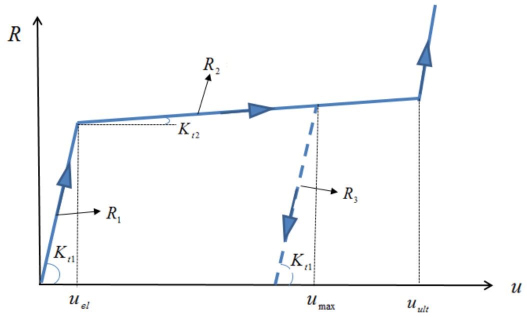

(b) Tube reaction curve in different phases

Fig. 11 Beam free body diagram and tube reaction curve

on the beam and x is the coordinate originating from one support.

$$p(x,t) = p_0 \cdot F(t) \cdot f(x) \tag{1}$$

For simplicity of derivation, it is assumed that both supports move spontaneously with the same displacements. The beam total displacement $Y(x,t)$ is the summation of support displacement $u(t)$ and beam deflection $y(x,t)$ as in Eq. (2), where $\Phi_i(x)$ is the i^{th} mode shape and $T_i(t)$ is its corresponding scalar in generalised space.

$$Y(x,t) = u(t) + y(x,t) = u(t) + \sum_{i=1}^{\infty} \phi_i(x) \cdot T_i(t) \tag{2}$$

The support displacement $u(t)$ is the rigid body motion mode of the beam and can be considered as the zeroth mode of the beam deflection. Under blast loading, the governing equation of beam vibration in its translational direction can be expressed as

$$EI\frac{\partial^4 Y}{\partial^4 x} + m\frac{\partial^2 Y}{\partial^2 t} = p(x,t) \tag{3}$$

where EI is the bending stiffness of the beam. Substituting Eq. (1) and Eq. (2) into Eq. (3) and simplifying with mode shape orthogonality yields

$$\int_0^l \Big[EI \sum_{i=1}^{\infty} \frac{d^4\phi_i(x)}{dx^4} T_i(t) + m\frac{d^2u(t)}{dt^2} + m\sum_{i=1}^{\infty}\frac{d^2T_i(t)}{dt^2}\phi_i(x) \\ - p(x,t) \Big] \cdot \phi_j(x)dx = 0, (i \neq j)$$

The governing equation of beam vibration takes the following form

$$T_i(t)\int_0^l f(x)\cdot\phi_i(x)dx + m\ddot{u}(t)\int_0^l \phi_i(x)dx \\ + m\ddot{T}_i(t)\int_0^l \phi_i^2(x)dx = p_0F(t)\int_0^l f(x)\phi_i(x)dx \tag{4}$$

A typical vapour cloud explosion in oil and gas industry generates a spherical blast wave front with small curvature. Thus, it is considered to be uniformly distributed over the beam span (i.e., $f(x)$ =1). Galerkin method is adopted to simplify Eq. (4) to be

$$\ddot{T}_i(t) + \omega_i^2 \cdot T_i(t) + m \cdot \omega_i^{\,2} \cdot \ddot{u}(t) = \omega_i^{\,2} \cdot p_0 \cdot F(t) \tag{5}$$

and

$$\omega_i^2 = \frac{\int_0^l f(x)\cdot\phi_i(x)dx}{m\int_0^l \phi_i^2(x)dx} \tag{6}$$

where ω_i is the i^{th} natural frequency of mode shape $\Phi_i(x)$.

According to Biggs (1964), rather than summation of an adequate number of characteristic vibration modes, the deflection of a beam subjected to uniformly distributed blast load can be represented by its deformed shape under a unit static uniformly distributed load as follows

$$\phi(x) = \frac{1}{12EI}\left(\frac{x^4}{2} - lx^3 + \frac{l^3x}{2}\right) \tag{7}$$

The blast loadings are often idealised as a triangle profile with zero rise time as shown in Fig. 10. Its mathematical expression is give in Eq. (8). It should be mentioned that the negative phase is normally neglected in engineering design.

$$F(t) \;=\begin{cases} 1 - t/t_d, & (0 \le t \le t_d) \\ 0, & (t > t_d) \end{cases} \tag{8}$$

With a free body diagram as shown in Fig. 11, the equation of motion of the left support is

$$V(0,t) - R = m_s \cdot \ddot{u}(t) \tag{9}$$

where $V(0,t)$ is the shear force at the left end of the beam and it takes the form of

$$V(0,t) = -EI\left.\frac{\partial^3 y(x,t)}{\partial x^3}\right|_{x=0} = \frac{l}{2}\cdot T(t) \tag{10}$$

R is the reaction from the translational supports, which is equivalent to the tube crushing force discussed earlier. The support reactions in the tube elastic, plastic crushing and unloading phases are denoted in Fig. 11 as R_1, R_2 and R_3 respectively, with analytical expressions of

$$R_1 = K_{t1} \cdot u \tag{11}$$

$$R_2 = K_{t2} \cdot u + (K_{t1} - K_{t2}) \cdot u_{el} \tag{12}$$

$$R_3 = K_{t1} \cdot u - (K_{t1} - K_{t2}) \cdot (u_{max} - u_{el}) \tag{13}$$

where u_{el} is the tube elastic limit; u_{ult} is the ultimate crushing limit when the tube is fully compressed; u_{max} is the maximum displacement when the tube stops and starts unloading (i.e., velocity $\dot{u}(t)=0$). Since the energy absorption capability is predominated by the tube plastic crushing phase, the behaviour after densification is not considered in this study. Reactions (i.e., R_1, R_2, R_3) shall be substituted in Eq. (9) along with the foam compression phases.

Combining Eq. (5) and Eq. (9) gives the forced vibration equations as in Eq. (14). Free vibration is a special case of the forced vibration when p_0 is zero.

$$\begin{cases} \ddot{T}(t)+\omega^2\cdot T(t)+m\omega^2\cdot\ddot{u}(t)=\omega^2 p_0\cdot(1-\dfrac{t}{t_d}) \\ m_s\cdot\ddot{u}(t)+R-\dfrac{l}{2}\cdot T(t)=0 \end{cases} \tag{14}$$

This is a set of linear nonhomogeneous 2nd order differential equations, the solutions are the summation of the general solutions of the homogeneous equations and the particular solutions of the nonhomogeneous equations. The solving process of Eq. (14) is briefed below by taking $R=R_1=K_{t1}\cdot u$ as example.

The homogeneous form of Eq. (14) is given in Eq. (15), by defining,

$$r=\frac{K_{t1}}{m_s},\quad \lambda=m\omega^2,\quad H=\frac{l}{2m_s}$$

$$\begin{cases} \ddot{T}(t)+\omega^2\cdot T(t)+\lambda\cdot\ddot{u}(t)=0 \\ \ddot{u}(t)+r\cdot u(t)-H\cdot T(t)=0 \end{cases} \tag{15}$$

Assume $u(t)=Ae^{st}$ and $T(t)=Be^{st}$, in which A and B are coefficients, are the general solutions for the homogeneous equations and substitute them in Eq. (15).

$$\begin{cases} \lambda\cdot A+(s^2+\omega^2)\cdot B=0 \\ (s^2+r)\cdot A-H\cdot B=0 \end{cases} \tag{16}$$

In order for the equations to have non-zero solutions, the coefficient matrix of A and B in Eq. (16) has to be zero.

$$(s^2+\omega^2)(s^2+r)+\lambda\cdot H=0$$

Solving for s produces four complex roots $s=\pm i\beta_1$ and $\pm i\beta_2$. With that the general solutions can be obtained by substituting s to the assumed $u(t)$ and $T(t)$ expressions. Particular solutions can be taken as any expressions that satisfy Eq. (14), for this example they are shown as the last terms of Eq. (17).

The complete solutions for Eq. (14) when $R=R_1$ are given in Eq. (17), in which A_1 - A_4 and B_1 - B_4 are undetermined coefficients.

$$\begin{cases} u(t)=A_1\sin(\beta_1 t)+A_2\cos(\beta_1 t)+ \\ A_3\sin(\beta_2 t)+A_4\cos(\beta_2 t)+\dfrac{p_0 l}{2K_{t1}}(1-t/t_d); \\ T(t)=B_1\sin(\beta_1 t)+B_2\cos(\beta_1 t)+ \\ B_3\sin(\beta_2 t)+B_4\cos(\beta_2 t)+p_0(1-t/t_d) \end{cases} \tag{17}$$

By substituting Eq. (17) to Eq. (14b), a relation between coefficient set A and B can be established, so that the number of undetermined coefficients can be reduced to four.

The at-rest initial conditions for this system of equations described below can be used to solve these coefficients with the assistance of a commercial software package called Mathematica.

$$u(0)=0,\dot{u}(0)=0,T(0)=0,\dot{T}(0)=0$$

Cautions shall be taken in the solving process that, with different R expressions, i.e., Eqs. (11)-(13), the particular solutions and the angular frequency β will vary.

Then, the beam mid-span deflection in elastic stage can be calculated as

$$y_{el}=\phi(\frac{l}{2})\cdot T(t) \tag{18}$$

3.1.3 Beam plastic stage

When at time $t=\tau$, beam mid-span bending moment $M(0.5L,\tau)$ is equal to the profiled blast wall panel's section plastic moment M_p, beam reaches the plastic stage.

The formulation for beam plastic stage is based on virtual work theory under the following two assumptions:

1) The plastic hinge length is assumed to be constant throughout the blast;

2) The support rotation angle θ is rigid-plastic after plastic hinge formation.

Assuming at the time instant $t=\tau$ ($\tau<t_d$), beam forms plastic hinge under blast loading. According to the virtual work theory, as shown in Fig. 12, summation of work of the internal and external forces done by virtual displacements $\delta\theta$ and δu is zero, thus

$$\int_0^{0.5l} p(x,t)\cdot\delta\theta\cdot xdx-\int_0^{0.5l} m(\ddot{\theta}\cdot x+\ddot{u})\cdot\delta\theta\cdot xdx \\ -M_{mid}\cdot\delta\theta-K_r\cdot\theta\cdot\delta\theta=0 \tag{19}$$

$$\int_0^{0.5l} p(x,t)\cdot\delta u\cdot dx-\int_0^{0.5l} m(\ddot{\theta}\cdot x+\ddot{u})\cdot\delta u\cdot dx \\ -(m_s\ddot{u}+R)\cdot\delta u=0 \tag{20}$$

The system of equations for beam plastic stage, i.e., Eq. (19) and Eq. (20), in the forced vibration phase ($\tau<t<t_d$) can then be simplified as Eq. (21). In free vibration phase ($t\geq t_d$), p_0 is zero.

$$\begin{cases} \dfrac{1}{24}ml^3\cdot\ddot{\theta}(t)-K_r\cdot\theta+\dfrac{1}{8}ml^2\cdot\ddot{u}(t)=\dfrac{1}{8}p_0 l^2(1-\dfrac{t}{t_d})-M_{mid} \\ (\dfrac{1}{2}ml+m_s)\cdot\ddot{u}(t)+R+\dfrac{1}{8}ml^2\cdot\ddot{\theta}(t)=\dfrac{1}{2}p_0 l(1-\dfrac{t}{t_d}) \end{cases} \tag{21}$$

Due to the law of continuity, the initial conditions of plastic stage are equal to the end conditions of elastic stage at time $t=\tau$, such that

$$u_0=u(\tau),\dot{u}_0=\dot{u}(\tau),\theta_0=0,\dot{\theta}_0=\dot{\theta}(\tau)$$

The initial rotational velocity at supports can be determined by the conservation of momentum, so that

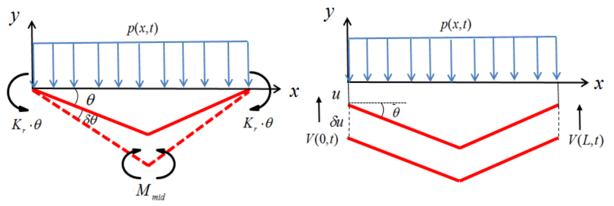

(a) Application of virtual work theory

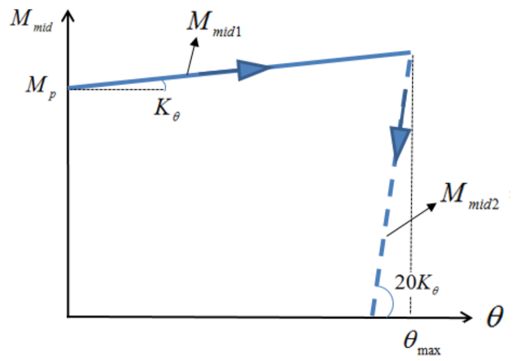

(b) Plastic moment curve at mid-span

Fig. 12 Virtual work theory and mid-span plastic moment behaviour curve

$$\int_0^l m\cdot\dot{y}(x,\tau)dx = 2m\int_0^{0.5l}\dot{\theta}_0\cdot xdx$$

$$\dot{\theta}_0 = \frac{p_0 l^3}{30EI}\dot{T}(\tau) \tag{22}$$

In Fig. 12, M_{mid} is the plastic bending moment at the mid-span of the beam. Since stainless steel has high ductility, the additional moment carried by the corrugated blast wall panel due to strain hardening is modelled by using a moment hardening parameter K_θ. M_{mid1} and M_{mid2} reflect the mid-span bending moment hardening and unloading behaviours.

K_θ was first introduced by Langdon and Schleyer (2005) to capture the buckling process of the beam. The solutions to the complex equations were too complicated to apply. The present study simplifies the procedure and specifies a moment unloading path as shown in Fig. 12. Thereby, both maximum and permanent deflections can be predicted by the analytical model. The formula for K_θ is derived from bending moment formula in Eq. (23),

$$M_{mid1} = \int(\sigma_y + E_h\kappa z)\cdot z\cdot dA = M_p + K_\theta\cdot\theta \tag{23}$$

where σ_y is the material yield stress (0.2% proof stress for stainless steel); E_h is the material hardening modulus assuming a linear strain hardening behaviour; z is the distance to the equal area axis; κ is the curvature at mid-span of the beam.

As the beam translational deflection increases, plastic hinge length will also develop. According to Nonaka (1967), the plastic hinge is assumed to have a length equals to the thickness of the plate at the onset of the plastic hinge formation (i.e., M=M_p, N=0) and further develop to be two times of the plate thickness when the beam reaches fully membrane state (i.e., M=0, N=N_p) whence the beam behaves as a string. Jones (1989) used the averaged value of the two extremes as a simplified approach to derive the threshold impulse for a beam rupture and compared favourably with experimental results. This study follows this simplified approach and assumes plastic hinge length to be 1.5 times of the plate thickness throughout the blast loading period. However, this assumption is made for rectangular sections. Considering the section has already formed plastic hinge in this stage, equivalent thickness t_{eq} is computed by equating the plastic section modulus Z_p of the corrugated section to a same width (W) rectangular section with the same magnitude. An example is given below and shown in Fig. 13 (Z_p is given in Table 2). This is the equivalent section method, which has been widely used in analytical modelling (Langdon and Schleyer 2005).

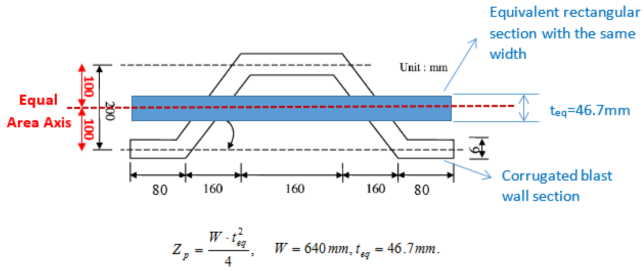

Fig. 13 Corrugated blast wall panel section

According to Jones (1989), κ can be expressed as Eq. (24), in which L_h is the plastic hinge length at mid-span. K_θ can be obtained by substituting Eq. (24) into Eq. (23).

$$\kappa = \frac{\theta}{L_h} = \frac{\theta}{1.5t_{eq}} \tag{24}$$

$$K_\theta = \frac{E_h\cdot I}{L_h} \tag{25}$$

The slope of the moment unloading curve is assumed to be close to the elastic stiffness of the beam. In this study, $20K_\theta$ is adopted for the following calculations and hence the moment unloading process is deduced to be

$$M_{mid2} = M_p + K_\theta\cdot\theta_{max} - 20\cdot K_\theta\cdot(\theta_{max} - \theta) \tag{26}$$

where θ_{max} is the maximum rotation at the support (i.e., angular velocity $\dot{\theta}$(t)=0).

Eq. (21) can then be solved in a similar manner to Eq. (14), accounting for varying expressions of R and M_{mid} in different phases. The continuity conditions are used at the transitions between different phases.

The maximum mid-span deflection of the beam is calculated to be

$$y_{max} = \phi(\frac{l}{2})\cdot T(\tau) + \theta_{max}\cdot\frac{l}{2} \tag{27}$$

3.1.4 Example problem

Table 2 Section and material properties of the blast wall panel

Section and material properties	Values &Units
Beam length L	3 m
Beam unit weight m	39.2 kg/m
Support weight m_s	10 kg
Cross section area A	4994 mm^2
Moment of Inertia I	2.95×10^7 mm^4
Plastic section modules Z_p	3.46×10^5 mm^3
Young's modulus E	200 GPa
Density ρ	7850 kg/m^3
Static yield stress (0.2% proof stress) σ_y	250 MPa
Dynamic yield stress (0.2% proof stress) σ_{dy}	316 MPa
Hardening modulus E_h	2.35 GPa

Table 3 Translational and rotational spring properties

Spring name	Translational spring K_t				Rotational spring K_r (kNm/rad)
	K_{t1} (kN/m)	K_{t2} (kN/m)	u_{el} (mm)	u_{ult} (mm)	
Spring for 1 bar	50200	1570	1	75	400
Spring for 2 bar	124000	3720	1	75	400
Spring for 3 bar	199000	6070	1	75	400

A single strip of the corrugated blast wall panel of 3 m long is taken as example to examine the analytical model and meanwhile evaluate the blast alleviation effects of the proposed system.

The panel sectional dimensions are given in Fig. 13. AISI316L stainless steel is adopted due to its good energy dissipation ability (Louca *et al*. 2004). The strain rate effect is taken into account by using the Cowper-Symonds relationship of

$$\frac{\sigma_{dy}}{\sigma_y} = 1 + \left(\frac{\dot{\varepsilon}}{D}\right)^{1/q} \tag{28}$$

where σ_{dy} is the dynamic yield stress at plastic strain rate $\dot{\varepsilon}$; σ_y is the static yield stress. The material constants D and q are coefficients for different materials. According to FABIG TN6 (2001), D=240 s^{-1} and q=4.74 are taken for AISI316L. A typical strain rate of 0.422 s^{-1} is adopted as an example in this study (Langdon and Schleyer 2004). Table 2 summarises the section and material properties of the blast wall panel.

The blast duration t_d is taken as 50 msec, which is a typical medium duration for a hydrocarbon explosion. Three blast overpressures, i.e., 1 bar, 2 bar and 3 bar (1 bar=100 kPa) are applied to test the performance. Generally, 1 bar is the typical overpressure for a strength level blast (SLB), and 3 bar can be taken as ductility level blast overpressure (DLB).

Ring stiffened tubes with a stiffener spacing of 100 mm (R1 type), 50 mm (R3 type) and 25 mm (R5 type) are placed along the overall width of the panel strip in the direction of blast incidence to resist the three blast

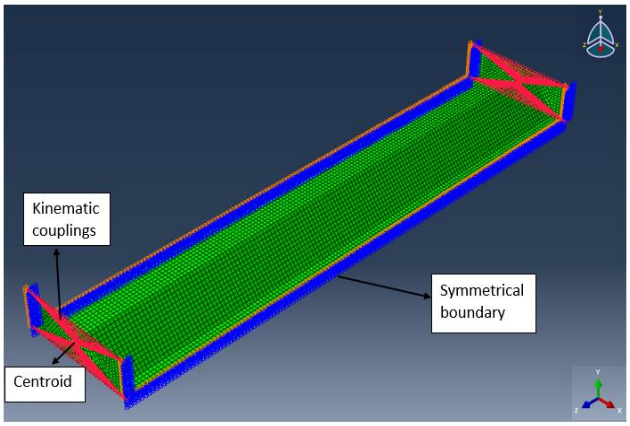

(a) Traditional design

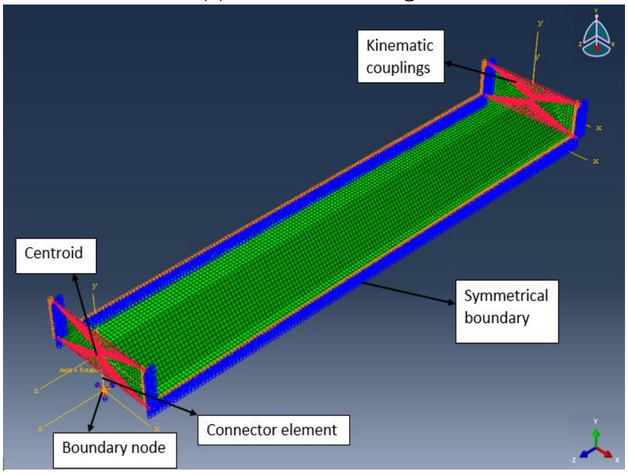

(b) Proposed design

Fig. 14 Boundary conditions for traditional and proposed design

overpressures respectively. The translational spring properties are derived from the tri-linear dash line approximation shown in Fig. 5 to Fig. 8, in which K_{t2} is taken as 1/30 of K_{t1}. The linear springs around the rotation core forms a push-pull mechanism which generates rotational stiffness. The rotational stiffness for these four overpressures are constant to be K_r=400 kNm/rad. A detailed description of the properties of translational and rotational springs is shown in Table 3.

3.2 Numerical modelling

3.2.1 Finite element model

Numerical analysis is applied to verify the analytical model presented above. The numerical simulation is implemented by using ABAQUS. One strip of corrugated blast wall panel with the same dimensions as analytical model is modelled with S4R elements. To balance simulation time with accuracy, mesh size 20 mm is adopted for the subsequent analysis. The FE blast wall model consists of 7121 elements.

In the traditional design, blast wall panels are fillet-welded to plate girder with end plates. Therefore, the assumption of simply supported conditions for the end connections should be sufficient for a preliminary design

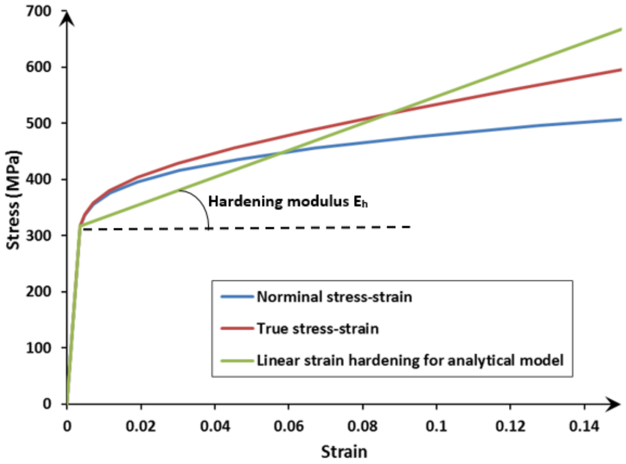

Fig. 15 Stress-strain curves for AISI316L stainless steel

(Louca *et al*. 2004). Kinematic couplings with all degrees of freedoms are applied by tying all the end nodes at both sides of the panel to the panel section centroid node to eliminate the possible numerical error introduced by additional moments caused by eccentricity (see Fig. 14(a)). Translations in three orthogonal directions (i.e., global UX, UY and UZ) of the centroid node are restrained. Thus, the numerical results and the analytical results are comparable. The corrugated edges of the panel are restrained in global UX, RY and RZ directions to form symmetrical boundaries, which renders the model to behave as a continuous panel.

For the proposed design, similar to Chen and Hao (2013) that used spring elements with derived force-displacement curves to simulate the behaviour of sandwich cores, the energy absorption supports are simplified as nonlinear springs using connector elements, which can simulate elastic, plastic, plastic unloading and stopping mechanisms. The connector element is used to link the centroid node of the end panel section where the vertical displacement (global UZ) is restrained, to boundary node where all degrees of freedom are fixed (see Fig. 14(b)).

3.2.2 Material properties

It is reported that the original Ramberg-Osgood expression, i.e., the first equation of Eq. (29), becomes seriously inaccurate beyond the 0.2% proof stress, and modifications has been made to adjust the formula based on experimental data (Rasmussen 2003). As the stress level of this example is expected to greatly exceed the proof stress in a DLB event, the modified Ramberg-Osgood expression (Rasmussen 2003) is applied to derive the nominal stress-strain relationships as follows,

$$\varepsilon = \begin{cases} \dfrac{\sigma}{E} - 0.002 \cdot \left(\dfrac{\sigma}{\sigma_{0.2}}\right)^{i}, & (\sigma \le \sigma_{0.2}) \\[2ex] \dfrac{(\sigma - \sigma_{0.2})}{E_{0.2}} + \varepsilon_u \left(\dfrac{\sigma - \sigma_{0.2}}{\sigma_u - \sigma_{0.2}}\right)^{j}, & (\sigma > \sigma_{0.2}) \end{cases} \qquad (29)$$

The material properties of AISI316L are given in Table 4 (Rasmussen 2003). The engineering stress-strain relationships are converted to true stress-strain to facilitate the computation in ABAQUS as indicated in Fig. 15. For the analytical derivation, the post-yield stress-strain relationship is simplified as a linear strain hardening with that the hardening modulus is obtained by curve fitting as shown in Fig. 15.

Table 4 Material parameters for AISI316L

Parameters	Values	Units
Initial young's modulus E	200	GPa
Tangent modulus at 0.2% strain $E_{0.2}$	23.541	GPa
Dynamic 0.2% proof stress $\sigma_{0.2}$	316	MPa
Ultimate plastic stress σ_u	616	MPa
Ultimate plastic strain ε_u	0.487	\
Strain hardening constant i	5.88	\
Strain hardening constant j	2.8	\

3.2.3 Loading and analysis

In order to compare results with the analytical model, the same blast loadings stated in Section 3.1.4 are applied to the FE model. The blast profiles are triangles with zero rise time, three peak overpressures (1 bar, 2 bar and 3 bar) with the same duration of 50 msec are analysed.

The blast loads are applied to all shell elements of the blast panel as distributed pressures normal to their faces by using the key word card *DLOAD.

For validation purpose, the imperfection and geometry nonlinearity are turn off in this stage. The analyses are performed in ABAQUS /Explicit package.

3.3 Results and discussion

3.3.1 Design requirements

This section performs a comparison study between the traditional and proposed design schemes against the current design code in the offshore industry to evaluate their performance. The performance based design philosophy is normally adopted for offshore blast wall designs (Fire and Explosion Guidance 2007). By analogy with earthquake assessments, the code requires the blast wall to be designed to sustain two level of events, strength level blast (SLB) and ductility level blast (DLB). The former represents a more frequent design event (10^{-3} exceedance per annual) where it is required that the blast walls shall not deform plastically and remain operational, while at the latter load level (10^{-4} to 10^{-5} exceedance per annual), plastic deformation is acceptable provided that blast walls remain in-place and the explosion event is not escalated. In order not to provoke escalation, the maximum wall deformation shall be limited to the minor of 300 mm and the clearance to critical equipment, pipelines and structural members located nearby to prevent collision. These criterions are applied to evaluate the performance of the proposed design concept.

3.3.2 Panel deflections

At the preliminary design stage, the blast wall deflection is the governing design consideration to determine the blast wall layout and select the profile section. Analytical method is normally adopted in this iterative design process as it is

Table 5 Summary of peak blast wall panel deflections

Blast cases	Traditional design		Proposed design		Reduction (by numerical)
	Numerical	Analytical	Numerical	Analytical	
1 bar	24.0 mm	23.8 mm	17.4 mm	16.2 mm	-24%
2 bar	110.5 mm	119.4 mm	66.6 mm	76.8 mm	-39%
3 bar	290.7 mm	278.7 mm	191.0 mm	201.4 mm	-34%

quicker and less expensive. In this study, in order to verify the effectiveness of the analytical model, the numerical results are compared to the analytical predictions in terms of panel deflection. Meanwhile, the dynamic structural responses of the proposed design are also compared with their counterparts from the traditional design to evaluate the performance.

Fig. 16 shows the blast wall panel mid-span deflection time-histories predicted by both analytical and numerical models for 1 bar traditional design case. As shown, the panel peak deflection predicted by ABAQUS is 24.0 mm (23.8 mm by analytical model). As no damping is applied, the panel keeps vibrating after the blast and the permanent deflections is observed to be 6 mm approximately, implying that larger sections are needed to satisfy the code requirements following the traditional design procedure, as it is specified in the design codes that blast wall shall not yield in a SLB event. The deflection time-histories and stress contour plots for 1 bar from the proposed design are shown in Fig. 16(b). It is observed that the centre point of the panel has a peak deflection of 17.4 mm numerically (16.2 mm analytically), which is 24% less compared to the traditional design. And almost no permanent deflection is observed as it vibrates around the zero displacement after the blast loading. In addition, due to the sliding effect, it is also observed that the time instant corresponding to the peak deflection has been delayed from 8 msec in traditional design to 15 msec in proposed design. Therefore, rather than switching to a larger section for the blast wall, the energy absorption supports can effectively mitigate the blast effects and render the blast wall deflection and stress to the code-compliant limits.

The structural responses of the deflection time-histories and stress contour plots for 2 bar and 3 bar cases are shown in Fig. 17 and Fig. 18 respectively. The peak deflections are 110.5 mm for 2 bar case and 290.7 mm for 3 bar case. The permanent deflections are almost the same as the peak deflections. As mentioned above, the code allowable deflection for blast wall design is 300 mm or the clearance to critical equipment, pipelines and structural members if they are located in the vicinity. Although the peak deflection for 3 bar case is 290.7 mm, which is approximately 10 mm less than the code-compliant limit, the collision risk is still high as offshore platforms or floating process units are very congested constructions. On the other hand, the peak deflections from the proposed design are 66.6 mm for 2 bar case and 191 mm for 3 bar case, which are generally 40% and 34% less respectively compared to the traditional designs. Especially for the 3 bar case, the proposed design cuts off the peak panel deflection by around 100 mm.

For the corroboration of the numerical and analytical

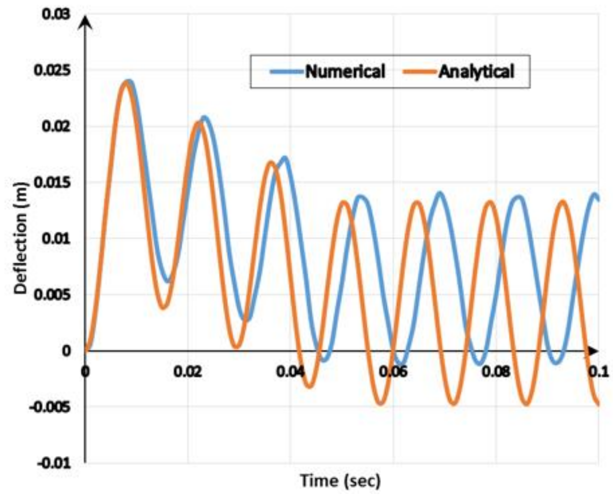

(a) Traditional design mid-span deflection

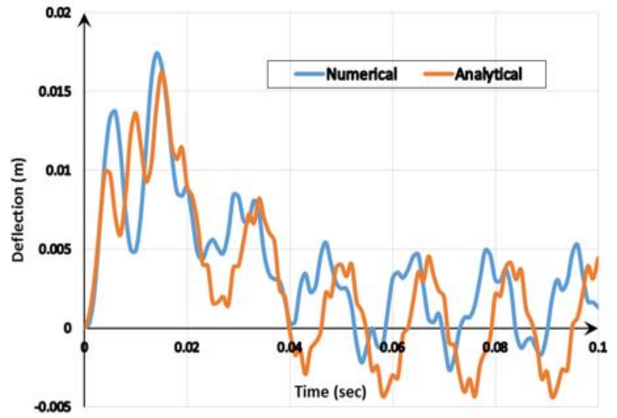

(b) Proposed design mid-span deflection

Fig. 16 Mid-span deflection time-history plots - 1 bar case

results, it is found that the correlations for 1 bar and 3 bar cases are relatively strong, and the analytical solutions can also capture the beam post-peak responses quite accurately. The differences of the peak deflections between the numerical and analytical results are less than 1% for 1 bar traditional design case, 7% for 1 bar proposed design case, and less than 5% for both 3 bar traditional and proposed design cases. However, it is noticed that the correlations are slightly weaker in the peak deflections for 2 bar cases. It could be caused by the simplification in material strain hardening modelling. In the analytical model, material is simplified to be bi-linearly with the post-yield behaviour to be linear strain hardening. Therefore, as shown in Fig. 15, with stress approaching 400 MPa (which is the peak stress of 2 bar case) the analytical material model gives larger strain than that from ABAQUS under the same stress, leading to around 10mm deflection difference between analytical and numerical results for 2 bar case. Nevertheless, for a quick hand calculation in the preliminary design stage, the difference is still acceptable. For the 3 bar traditional design case, a different pattern from the other two examples is observed that the peak deflection predicted by analytical model is slightly less than the numerical result. Similar explanation can apply here as the peak stress has climbed over 520 MPa, which has

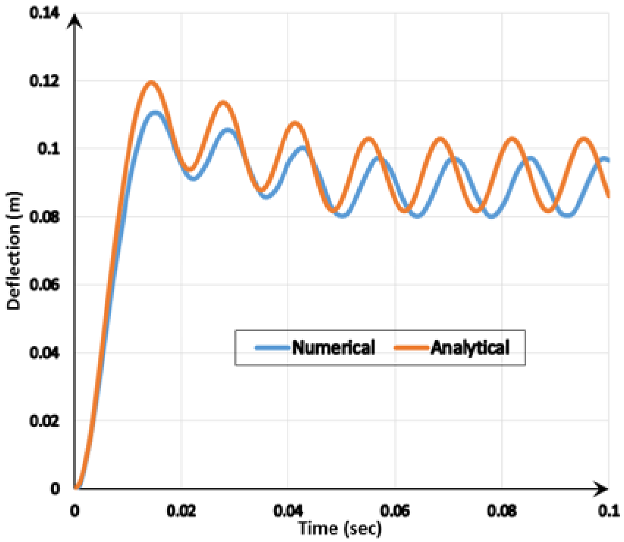

(a) Traditional design mid-span deflection

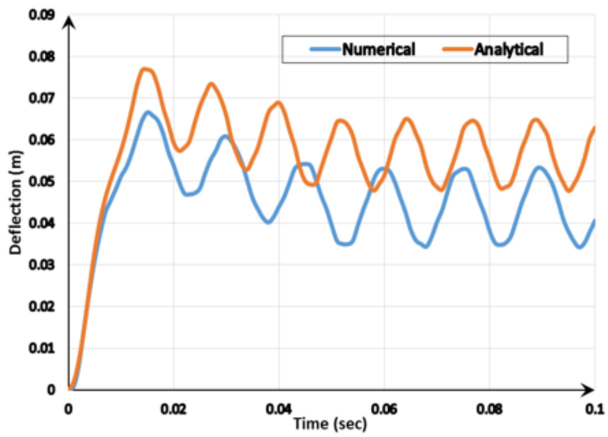

(b) Proposed design mid-span deflection

Fig. 17 Mid-span deflection time-history plots - 2 bar case

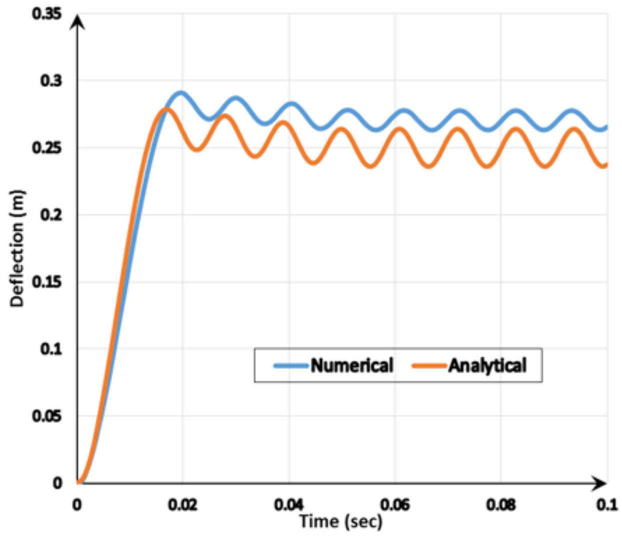

(a) Traditional design mid-span deflection

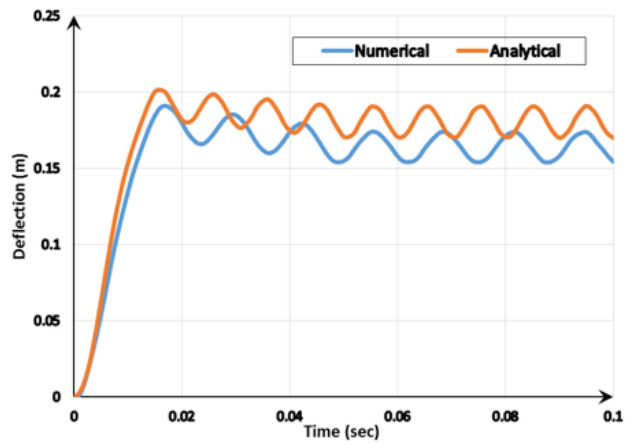

(b) Proposed design mid-span deflection

Fig. 18 Mid-span deflection time-history plots - 3 bar case

passed the crossing point between the ABAQUS and analytical material model, so that the mechanism is reversed. Another reason for the under-prediction is that the plastic hinge length is assumed to be constant ($1.5t_{eq}$) throughout the analysis, however, in reality the plastic length can further develop especially under strong blasts more than 3 bar. Thus, the assumption of an averaged plastic hinge length $1.5t_{eq}$ may over-estimate the moment hardening for strong blasts and hence under-predict the peak deflection. More effort is required to incorporate varying plastic hinge length with time in the analytical model, but it is out of the scope of the current study.

Table 5 summarises the peak deflections for both the traditional and proposed designs. The reasonable agreements between analytical and numerical solutions not only validate the analytical model presented above, but also demonstrate the blast alleviation capability of the proposed design.

3.3.3 Energy absorption

From the perspective of energy absorption, the explosion energy is transferred to the blast wall as it displaces and deforms. Neglecting the energy loss, the total energy E_t input to the structure system (i.e. work of external forces) is transformed into a summation of the kinetic energy E_k and the internal energy E_i (i.e. strain energy) of the system. The kinetic energy is minimal and it quickly decreases to zero with time, while the internal energy of the system increases to absorb the blast energy.

For traditional design, as the only component, the blast wall panel takes up all the input energy, while with the proposed design, the total energy is dissipated by different components. Fig. 19 compares the internal energy absorbed by different structural components for all three case, with the percentages of energy absorption labelled above the bar charts. For 1 bar case, as the loading is relative small compared to the panel bending stiffness, the primary deformation mode of the blast wall is similar to a rigid body movement, hence the majority of the energy is absorbed by tube deformation (80%). However, with the increase of blast overpressures, the primary deformation mode has shifted to bending, therefore, the energy absorption by the tubes tends to decrease. Especially for 3 bar case, the energy absorption contribution of tubes drops to 15%, this is because the plastic hinge forms too early (at 2.5 msec), at which the support displacement is only 0.74 mm less than

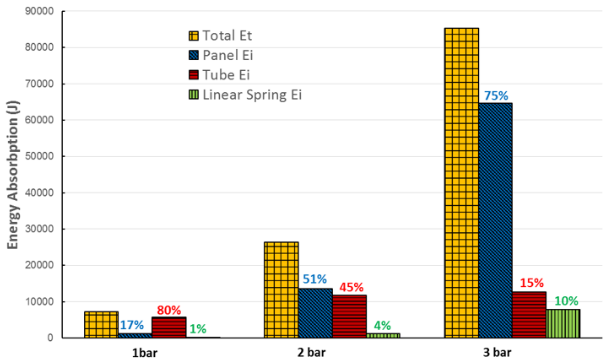

Fig. 19 Comparison of energy absorption of various components

the elastic limit of 1 mm. As a result, it is easier for the panel to bend and attract more energy.

On the other hand, the energy absorbed by the linear springs rises with stronger blasts, up to 10% in 3 bar case. Since panel permanent deflection has occurred, linear rotational springs are not able to release energy to restore to their original positions. Therefore, the linear rotational springs have become energy absorbers as well.

In summary, the tubes together with the linear springs absorb around 50% of the input energy for 2 bar and 25% for 3 bar case.

4. Conclusions

This study investigates the energy absorption performance of a simpler, lighter but more efficient energy absorber called the ring stiffened tube. Due to the increase of section modulus in tube wall and restraining effect of the stiffener flange, key energy absorption parameters (PCF, EA and SEA) have been significantly improved compared to an empty tube.

The potential application of the ring stiffened tubes in the blast wall design has also been investigated. It is proposed to replace blast wall endplates at the supports with energy absorption devices made up by ring stiffened tubes and springs. An analytical model of the proposed system is developed and then collaborated with the numerical findings. The predictions with analytical model are in reasonable agreement with numerical simulations, which validates the analytical model as a quick assessment tool for the deflection estimation in the preliminary design stage. Further comparisons to the traditional design also give credit to its blast alleviation capability as the peak panel deflections are reduced by almost 40%.

References

Al-Rifaie, H. and Sumelka, W. (2017), “Numerical analysis of reaction forces in blast resistant gates”, *Struct. Eng. Mech.*, **63**(3), 347-359.

Biggs, J.M. (1964), *Introduction to Structural Dynamics*, McGraw-Hill, London, U.K.

Chen, W. and Hao, H. (2013), “Numerical study of blast-resistant sandwich panels with rotational friction dampers”, *Int. J. Struct. Stab. Dyn.*, **13**(5) 1350014.

Chen, W.X., Gao, Z.K. and Ye, J.H. (2011), “Dynamic responses and failure modes of reinforced concrete beam with flexible supports under blast loading”, *ACTA ARMAMENTARII*, **23**(10), 1271-1277.

DNV-RP-C208 (2013), *Determination of Structural Capacity by Non-Linear FE analysis Methods*, Det Norske Veritas (DNV), Høvik, Norway.

Eyvazian, A., Habibi, M.K., Hamouda, A.G. and Hedayati, R. (2014), “Axial crushing behaviour and energy absorption efficiency of corrugated tubes”, *Mater. Des.*, **54**, 1028-1038.

FABIG TN6 (2001), *Technical Note 6: Design Guide for Steels at Elevated Temperatures and High Strain Rates*, Fire and Blast Information Group (FABIG), Berkshire, U.K.

Fan, Z., Shen, J., Lu, G. and Ruan, D. (2013), “Dynamic lateral crushing of empty and sandwich tubes”, *Int. J. Imp. Eng.*, **53**, 3-16.

Fire and Explosion Guidance (2007), *Oil and Gas UK*, London, U.K.

Jones, N. (1989), *Structural Impact*, Cambridge University Press, Cambridge, U.K.

Langdon, G.S. and Schleyer, G.K. (2005), “Inelastic deformation and failure of profiled stainless steel blast wall panels part II: Analytical modelling considerations”, *Int. J. Imp. Eng.*, **31**(4), 371-399.

Langdon, G.S. and Schleyer, G.K. (2004), “Unusual strain rate sensitive behaviour of AISI 316L austenitic stainless steel”, *J. Strain. Analy. Eng.*, **39**(1), 71-86.

Louca, L.A., Boh, J.W. and Choo, Y.S. (2004), “Design and analysis of stainless steel profiled blast barriers”, *J. Constr. Steel Res.*, **60**(12), 1699-1723.

Lu, G. and Yu, T. (2003), *Energy Absorption of Structures and Materials*, Woodhead Publishing Limited, Cambridge, U.K.

Meng, F., Zhang, B., Zhao, Z., Xu, Y., Fan, H. and Jin, F. (2016), “A novel all-composite blast-resistant door structure with hierarchical stiffeners”, *Compos. Struct.*, **148**, 113-126.

Menkes, S. and Opat, H. (1973), “Broken beams-tearing and shear failures in explosive loaded clamped beams”, *Exp. Mech.*, **3**, 480-486.

Nonaka, T. (1967), “Some interaction effects in a problem of plastic beam dynamics”, *J. Appl. Mech.*, **34**(3), 623-643.

Nouri, M.D., Hatami, H. and Jahromi, A.G. (2015), “Experimental and numerical investigation of expanded metal tube absorber under axial impact loading”, *Struct. Eng. Mech.*, **51**(6), 1245-1266.

Rasmussen, K.J.R. (2003), “Full-range stress-strain curves for stainless steel alloys”, *J. Constr. Steel Res.*, **59**(1), 47-61.

SIMULIA (2015), *Abaqus Analysis User’s Guild*, v.6.14.

Song, C.M., Wang, M.Y. and Liu, B. (2014), “Effects of boundary restrains on dynamic response of a beam under blast loading (I)-theoretical study and analysis”, *J. Vibr. Shock*, **33**(5), 82-86.

Wang, H., Yang, J., Liu, H., Sun, Y. and Yu, T.X. (2015), “Internally nested circular tube system subjected to lateral impact loading”, *Thin Wall Struct.*, **91**, 72-81.

Xia, Z., Wang, X., Fan, H., Li, Y. and Jin, F. (2016), “Blast resistance of metallic tube-core sandwich panels”, *Int. J. Imp. Eng.*, **97**, 10-28.

Xiang, X.M., Lu, G., Ma, G.W., Li, X.Y. and Shu, D.W. (2016), “Blast response of sandwich beams with thin-walled tubes as core”, *Eng. Struct.*, **127**, 40-48.

Zhang, B., Jin, F., Zhao, Z., Zhou, Z., Xu, Y., Chen, H. and Fan, H. (2018), “Hierarchical anisogrid stiffened composite panel subjected to blast loading: Equivalent theory”, *Compos. Struct.*, **187**, 259-268.

Zhang, B., Nian, X., Jin, F., Xia, Z. and Fan, H. (2016), “Failure analyses of flexible ultra-high molecular weight polyethylene

(UHMWPE) fiber reinforced anti-blast wall under explosion", *Compos. Struct.*, **184**, 759-774.

CC